Article

Synthesis and Characterization of Hematite, Magnetite and Maghemite Supported on Silica Gel

P. A. Chernavskiy [1,2,3], A. A. Novakova [4,*], G. V. Pankina [1,3], D. A. Pankratov [1], S. I. Panfilov [4] and G. A. Petrovskaya [4]

[1] Department of Chemistry, Lomonosov Moscow State University, 1-3 Leninskie Gory, Moscow 119991, Russia; chern5@inbox.ru (P.A.C.); pankina5151@inbox.ru (G.V.P.); pankratov@radio.chem.msu.ru (D.A.P.)
[2] Zelinsky Institute of Organic Chemistry, Russian Academy of Sciences, Moscow 170100, Russia
[3] Topchiev Institute of Petrochemical Synthesis, Russian Academy of Sciences, Moscow 119071, Russia
[4] Faculty of Physics, Lomonosov Moscow State University, 1-2 Leninskie Gory, Moscow 119991, Russia; panfilov.si23@physics.msu.ru (S.I.P.); petrovskaya@physics.msu.ru (G.A.P.)
[*] Correspondence: novakova.alla@gmail.com

Abstract: A new method for obtaining nanosized particles of iron oxides using porous silica gel is proposed. In situ magnetometry was used to study the reduction of hematite deposited on silica gel during the thermolysis of glucose. The formed magnetite and maghemite obtained by subsequent oxidation of the magnetite were studied using X-ray diffraction and Mossbauer spectroscopy. It was shown that both the size of the oxide particles and the phase composition significantly depended on the porous structure of the silica gel. In particular, the formation of superparamagnetic maghemite particles on silica gels with pore sizes of 30, 15 and 10 nm was demonstrated.

Keywords: maghemite nanoparticles; iron oxides; silica gel; X-ray diffraction; Mossbauer spectroscopy; magnetic measurements

1. Introduction

Materials containing nanosized particles of iron oxides are widely used in various fields, from catalysis to medicine [1–4]. First of all, nanosized particles of iron-containing substances are of interest for fundamental scientific research due to the differences in the physical properties of bulk and nanosized materials [5,6]. For example, synthetic nanosized magnetite has been proposed as a potential reactant for the purification of polluted groundwater and as an effective sorbent of metalloid pollutants due to its high surface area [7,8].

The targeted synthesis of preparations containing pure single-phase nanosized particles of iron with a monodisperse size distribution encounters significant difficulties due to the diversity of iron chemistry, which manifests itself in the stability of two oxidation states and rich crystal chemistry. All this causes problems with the coexistence of oxides of different compositions in one preparation, for example, such as magnetite (Fe_3O_4), maghemite (γ-Fe_2O_3), hematite (α-Fe_2O_3) and wustite (FeO) [9,10]. This problem is exacerbated by the tendency of nanosized iron oxide particles to aggregate into large agglomerates. This is especially important when working with magnetic particles such as Fe_3O_4 and γ-Fe_2O_3 [11]. To prevent particle aggregation, synthesis methods are used in carrier matrices, in particular, on silica gel. Silica was shown to be the best support in terms of both activity and selectivity in various catalytic reactions and, in particular, in Fisher–Tropsch synthesis [12–16].

Most often, to obtain such nanosized iron-containing preparations in a silica gel matrix, the sol–gel synthesis technique is used [9]. However, as a rule, as a result of using the sol–gel method, the synthesized nanoparticles of iron oxides are encapsulated in the bulk of the silica gel. In this case, the surfaces of the iron oxide nanoparticles are inevitably covered with silica shells and have limited access to the adsorbate. Such composites are not

effective for catalysis due to the limited number of active sites accessible to reagents on the surface. In addition, it is necessary to take into account the possibility of the interaction of iron oxides with the silica gel material, especially at low iron concentrations [5].

Nanoparticles of iron oxides on silica gel can be prepared by impregnating the carrier with a solution of iron nitrate followed by thermolysis of the nitrate. This method is often used to prepare iron-supported catalysts [1,7]. Sonochemical synthesis of silica-supported iron oxide nanostructures was used by the authors of one work [17]. Preparation of magnetite on silica is a more difficult task, since the direct reduction of supported hematite inevitably leads to a mixture of oxides: Fe_2O_3, Fe_3O_4, FeO. To reduce hematite, it is possible to use hydrocarbons, as well as various carbohydrates. In this case, it is possible to channel the reaction towards the exclusive formation of magnetite [18]. The synthesis of ultrafine particles of magnetite using polysaccharides as a reducing agent was proposed in [19]. Silica-supported maghemite was prepared through the pyrolysis of a ternary composite of poly (vinyl alcohol) (PVA), iron (III) hydroxide and silica gel, and was characterized using X-ray diffraction and infrared spectroscopic and BET surface area measurements [20,21]. The synthesis of γ-Fe_2O_3 particles and the investigation of their properties are of fundamental importance for the development of science and technology. The preparation of pure γ-Fe_2O_3 nanophase presents some difficulties arising from the different metal oxidation states, which can lead to the presence of various oxides. The method of controlled oxidation of magnetite is usually used to obtain magnetite [11].

The aim of the present study is to demonstrate a technique for the selective synthesis of magnetite nanoparticles by means of the reduction of hematite supported on silica gel with pores of various sizes using glucose pyrolysis products, which makes it possible to synthesize nanosized maghemite particles of various specified sizes. The physicochemical properties of all of the synthesized composites were confirmed using Mossbauer spectroscopy, X-ray phase analysis and magnetic methods. Since the composites synthesized according to the method proposed in this work are supposed to be used as catalysts in the future, we refer to them as catalysts in what follows.

2. Materials and Methods

2.1. Materials

Iron (III) nitrate nonahydrate (Sigma-Aldrich, St Louis, MO, USA) ($Fe(NO_3)_3 \cdot 9H_2O$) was used as a precursor. CARIACT silica gel with grades of Q-30, Q-15 and Q-10 (Q-X, where X = 30, 15, 10 nm as the average pore size in silica gel, with surface areas of 100, 200 and 300 m^2/g, respectively) manufactured by Fuji Silysia Chemical, Ltd. (Nagoya, Japan) was used as a support. The nominal content of iron was 20 mass% for Q-30 and 15 mass% for Q-15 and Q-10.
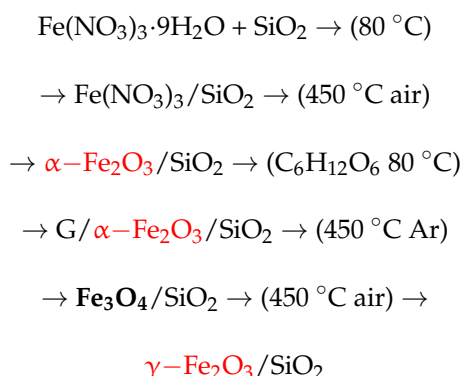
Catalysts were prepared via incipient wetness impregnation of the support with aqueous solutions of hydrous iron nitrate. After impregnation, the catalysts were dried in a rotary evaporator at 80 °C for 2 h. Then, they were calcined in air at 450 °C for 4 h with temperature ramping of 10 °C/min. These samples were denoted as Fe_2O_3/Q-30, Fe_2O_3/Q-15 and Fe_2O_3/Q-10.

Obtained Fe_2O_3/Q samples (calcined at 450 °C) were additionally impregnated with an aqueous glucose solution at room temperature and dried in a rotary evaporator at 80 °C. The iron/glucose molar ratio was 10/1.

These samples were denoted as G/Fe_2O_3/Q-30, G/Fe_2O_3/Q-15 and G/Fe_2O_3/Q-10.

Subsequently, some of the catalysts were studied using the in situ magnetic method, and some were subjected to calcination in an argon current at a heating rate of 10 °C/min to a temperature of 450 °C for 4 h. The catalysts obtained from calcination in argon were designated as Fe_3O_4/Q-30, Fe_3O_4/Q-15 and Fe_3O_4/Q-10. Some of the catalysts obtained in this way were subjected to oxidation in an air current at 450 °C. The resulting oxidation

catalysts were designated as $\gamma\text{-}Fe_2O_3$/Q-30, $\gamma\text{-}Fe_2O_3$/Q-15 and $\gamma\text{-}Fe_2O_3$/Q-10. A block diagram of the sequence of operations in the synthesis of catalysts is presented below.

$$Fe(NO_3)_3 \cdot 9H_2O + SiO_2 \rightarrow (80\,^\circ C)$$

$$\rightarrow Fe(NO_3)_3/SiO_2 \rightarrow (450\,^\circ C\ air)$$

$$\rightarrow \alpha{-}Fe_2O_3/SiO_2 \rightarrow (C_6H_{12}O_6\ 80\,^\circ C)$$

$$\rightarrow G/\alpha{-}Fe_2O_3/SiO_2 \rightarrow (450\,^\circ C\ Ar)$$

$$\rightarrow \mathbf{Fe_3O_4}/SiO_2 \rightarrow (450\,^\circ C\ air) \rightarrow$$

$$\gamma{-}Fe_2O_3/SiO_2$$

2.2. X-ray Diffraction Study

The X-ray diffraction experiment was performed on a PANalytical Empyrean diffractometer. The immobile sample, in the form of a powder layer of 1 mm thick and about 20 mm in diameter on a non-reflective holder, was placed in the center of the vertical plane of the goniometer. The experiment was carried out in "Θ–Θ" geometry with synchronous movement of the PIXcel-3D detector and the ceramic X-ray tube along the goniometric circle. Diffraction patterns were measured on Cu Kα radiation in the scanning range for angle 2Θ of 5–100 degrees.

Mathematical processing of diffraction patterns, quantitative phase analysis of the samples (according to the Chung method) and particle size estimations using the Scherer method were carried out using the HighScore Plus program (version 4.9) and the JSCD file cabinet.

2.3. Mossbauer Spectroscopy

Mossbauer absorption spectra were obtained on an MS1104EM Express Mossbauer spectrometer (Cordon GmbH, Rostov-on-Don, Russia) in the constant acceleration mode with the triangular velocity reference signal. The 57Co nuclei in a metal rhodium matrix (RITVERC GmbH, St. Petersburg, Russia) with 50 mCi activity were used as the γ-radiation source. The spectra were obtained at room temperature (23 $\pm$ 3 °C). Mathematical processing was carried out for spectra using UNIVEM (Rostov-on-Don State University, Russia) software with a high resolution (1024 points). Experimental data were fitted using a superposition of symmetrical doublets and sextets with fixed line widths and intensity ratios. The chemical shifts were determined relative to α-Fe.

2.4. Magnetic Studies

Magnetic studies of the samples were carried out on a vibration magnetometer using the in situ regime. The test sample (10 mg) was placed in a measuring cell of the vibrating magnetometer [22], which is a flow-through microreactor with an internal volume of 0.3 cm^3. The test sample was clamped between two membranes of porous quartz. In a nonisothermal experiment, the sample was heated (10 °C/min) to a predetermined temperature in the Ar or air at a magnetic field strength of 3 kOe with a flow rate of 10 cm^3/min, while a change in magnetization was recorded continuously at a frequency of 1 Hz.

3. Results

Catalysts Fe_2O_3/Q-30, Fe_2O_3/Q-15 and Fe_2O_3/Q-10 did not reveal any changes in magnetization in an argon current up to the temperature of T = 600 °C. However, the exposure of catalysts G/Fe_2O_3/Q-30, G/Fe_2O_3/Q-15 and G/Fe_2O_3/Q-10 under identical conditions showed an increase in magnetization starting from 270 °C. Figure 1 shows the
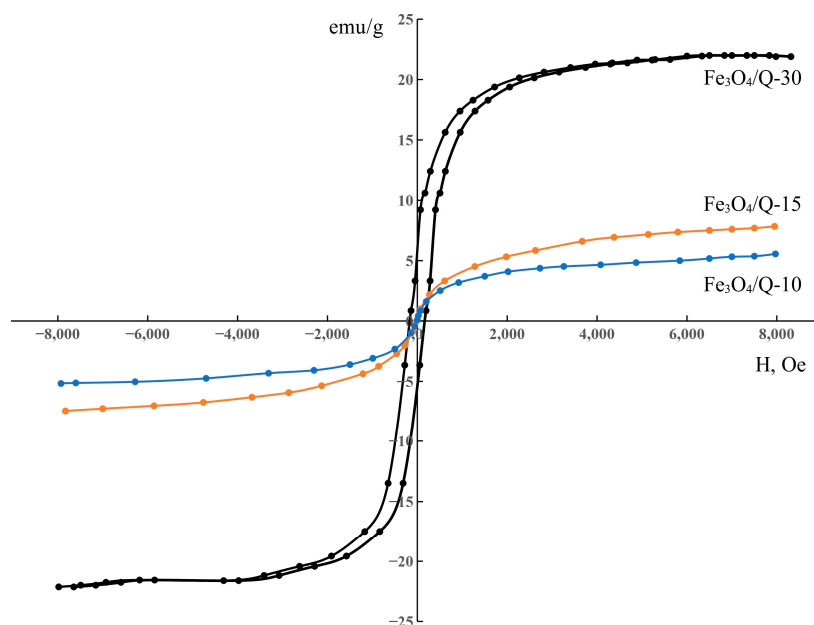
dependence of magnetization on temperature for the catalysts during heating in argon. The growth of magnetization is due to pyrolysis of glucose. During pyrolysis, the emitted CO reduces hematite particles to magnetite through the following reaction:

$$3Fe_2O_3 + CO = 2Fe_3O_4 + CO_2$$
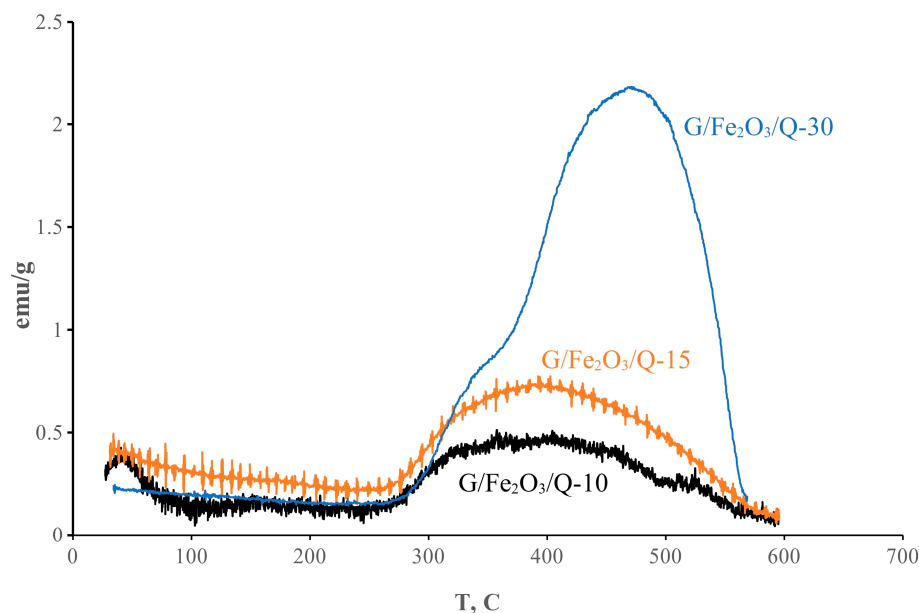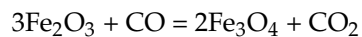
Figure 1. The dependence of magnetization on temperature for catalysts during heating in argon.

At temperatures above 500 °C, glucose is completely transformed into a mixture of CO, CO_2 and H_2O.

The drop in magnetization to zero at T = 570–580 °C corresponds to the Curie temperature of magnetite. After cooling, the dependences of magnetization on the field were measured, and the results are shown in Figure 2.

Figure 2. The dependences of magnetization on the field for catalysts $Fe_3O_4/Q-30$, $Fe_3O_4/Q-15$ and $Fe_3O_4/Q-10$.

Note the absence of remanent magnetization and coercive force in the case of catalysts Fe_3O_4/Q-15 and Fe_3O_4/Q-10. This indicates the presence of superparamagnetism in these catalysts at room T. The presence of superparamagnetic particles allowed us to estimate the size of the particles using the Langevin equation. In this way, it was possible to estimate the upper and lower limits of Fe_3O_4 particle size, d, using the low-field (d_{LF}) and high-field field (d_{HF}) approximations of the Langevin function [23], as follows:

$$d_{LF}^3 = \frac{18k}{\pi Is}\left(\frac{\sigma}{\sigma_s}\right) \Big/ \left(\frac{H}{T_m}\right) \tag{1}$$

$$d_{HF}^3 = \frac{6k}{\pi I_s}\left[1 - \left(\frac{\sigma}{\sigma_s}\right)\right]^{-1} \Big/ \left(\frac{H}{T_m}\right) \tag{2}$$

where k is the Boltzmann constant and I_s is the spontaneous magnetization per unit volume for the bulk Fe_3O_4 saturation magnetization of the test sample at 93 K.

The saturation magnetization (I_s) was estimated by plotting emu/g versus $1/H$ and extrapolating to zero, as shown in Figure 3.
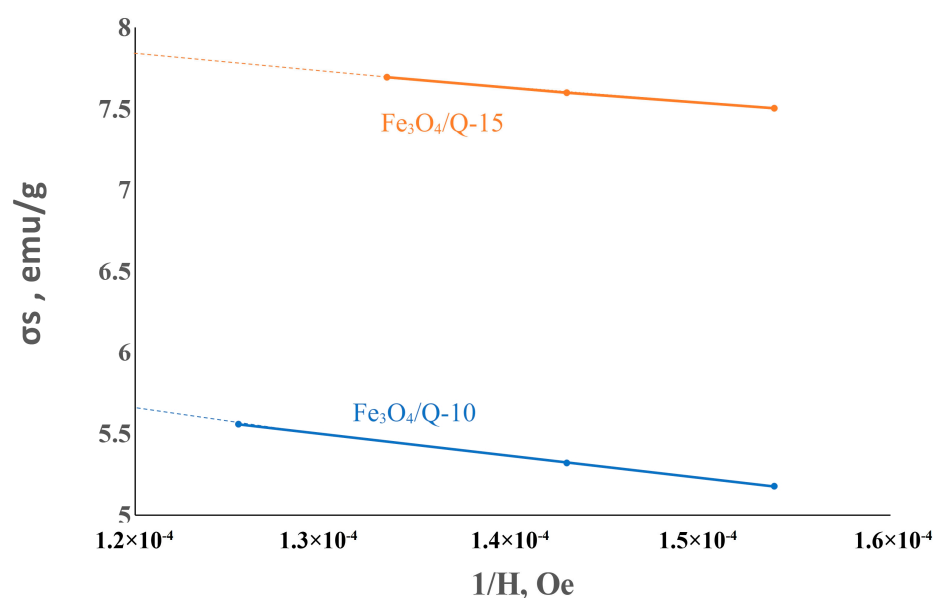
Figure 3. Saturation magnetization determination: extrapolation at $1/H = 0$ of the magnetizations of Fe_3O_4/Q-15 and Fe_3O_4/Q-10.

The saturation magnetization of bulk magnetite (I_s) was assumed to be 70 emu/g [24–27]. Table 1 shows the values of max. and min. particle size that were calculated using equations 1 and 2, as well as the average size of catalysts Fe_3O_4/Q-15 and Fe_3O_4/Q-10.

Table 1. The upper and lower limits of Fe_3O_4 particle size (d), estimated for each case.

Medium, nm	d (max)	d (min)	Catalysts
5.7	7 nm	4.5 nm	Fe_3O_4/Q-15
5.4	7 nm	3.8 nm	Fe_3O_4/Q-10

After oxidation in air at 450 °C, catalysts Fe_3O_4/Q-30, Fe_3O_4/Q-15 and Fe_3O_4/Q-10 acquired a red-orange color and remained magnetized at room temperature. We assume that magnetite oxidation results in the formation of maghemite.

If the system contains no multidomain particles, the particle size distribution can be analyzed using the following equation [23]:

$$\gamma = 1 - 2Jr/Js \tag{3}$$

where γ is the proportion of superparamagnetic particles and Jr is the saturation remanent magnetization.

According to the XRD data (given below), the maghemite particles in the catalysts were smaller than the single-domain size of 40 nm [25].

More detailed information about the composition of the systems under study was provided with X-ray phase analysis. The results of the X-ray phase analysis for all of the investigated objects are given below.

The X-ray diffraction patterns of all the samples at the first stage of synthesis (Figures 4–6) were a superposition of reflections from two phases: a single, very wide and intense reflex of SiO_2 gel (111) and a system of lines of nanosized α-Fe_2O_3 phase.

On the diffraction patterns obtained, at the stages of transition from hematite to magnetite and, further, to maghemite, the intensity of the reflections of the forming Fe_3O_4 and γ-Fe_2O_3 phases increased, and the reflections themselves became narrower in comparison with the reflections of γ-Fe_2O_3. This indicates an increase in the size of the obtained Fe_3O_4 and γ-Fe_2O_3 nanoparticles within the pore size throughout synthesis.
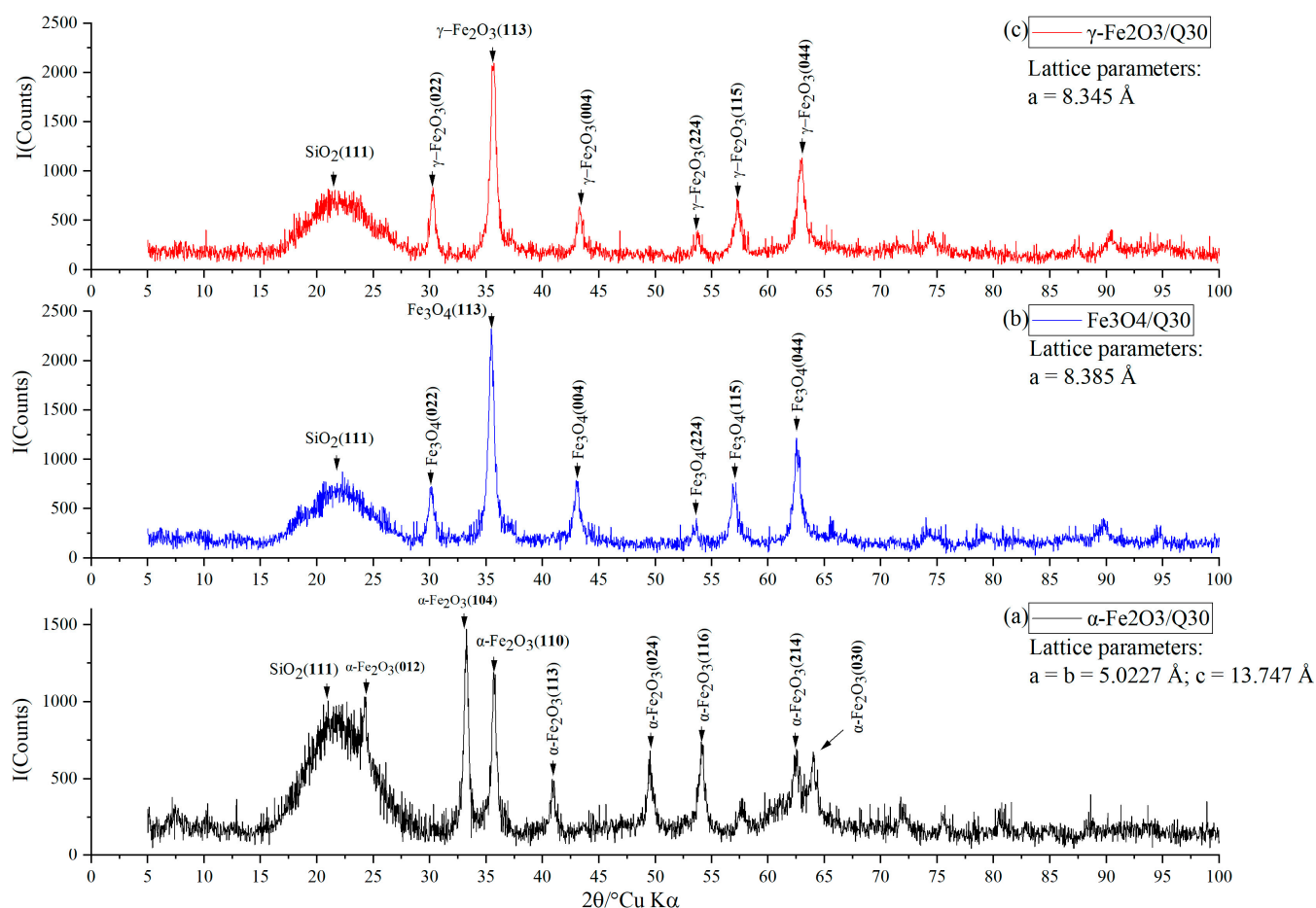
Figure 4. Diffraction patterns of catalysts (**a**) α-Fe_2O_3/Q-10, (**b**) Fe_3O_4/Q-10 and (**c**) γ-Fe_2O_3/Q-10.
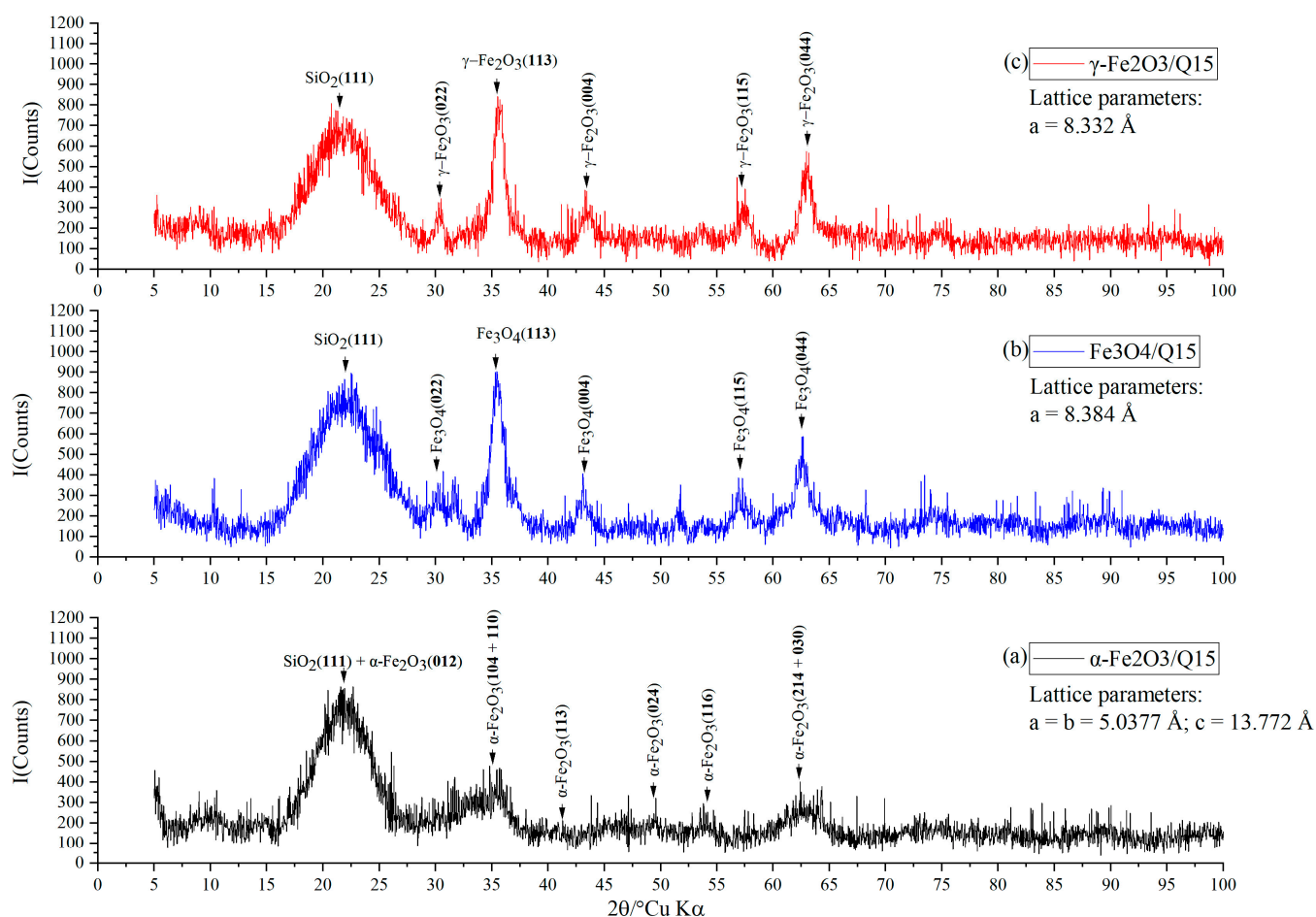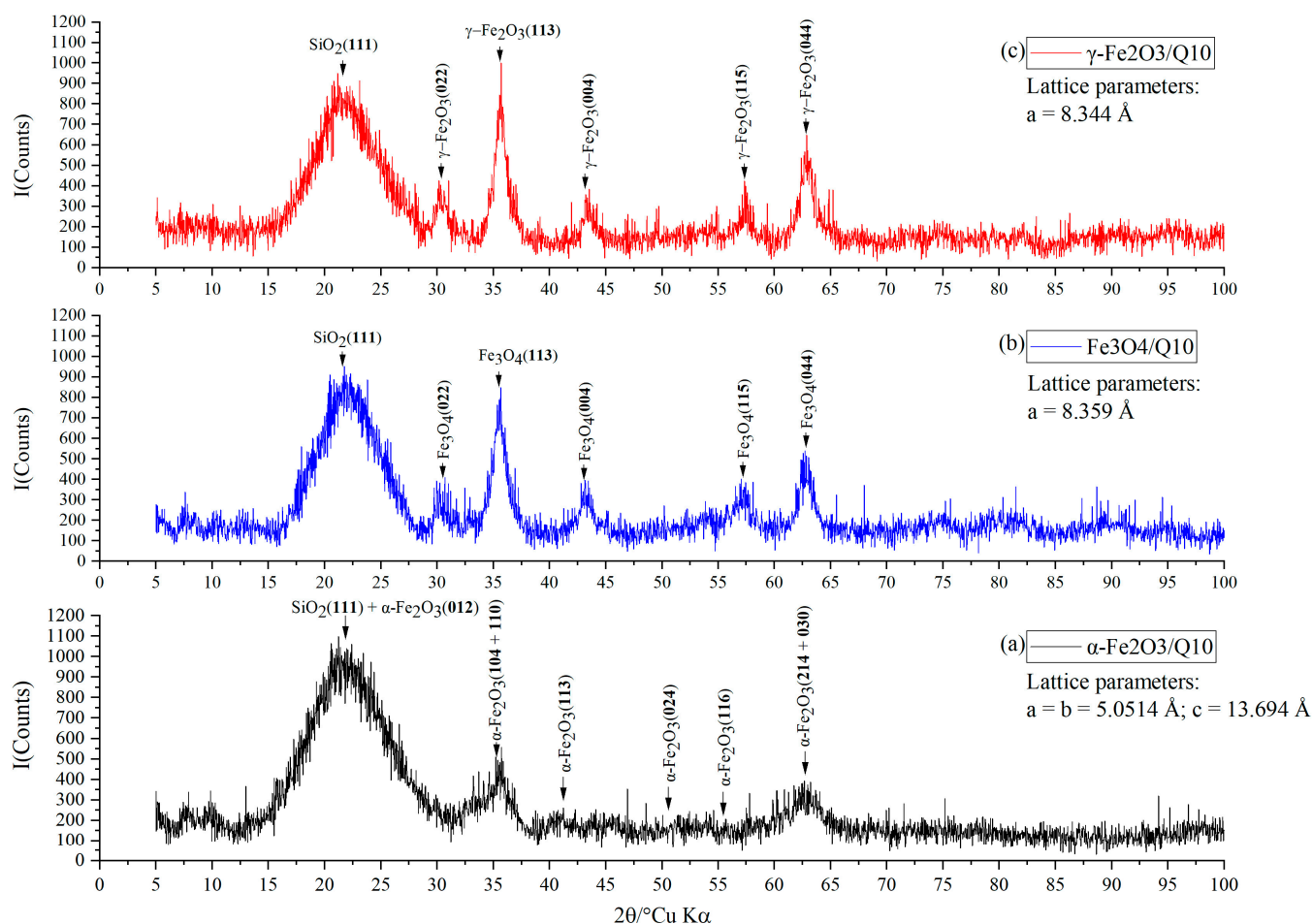
Figure 5. Diffraction patterns of catalysts (**a**) α-Fe_2O_3/Q-15, (**b**) Fe_3O_4/Q-15, (**c**) γ-Fe_2O_3/Q-15.

The mean particle sizes in the silica gel pores that were determined using the Scherrer method are given in Table 2. The average particle sizes given in the table agree well with the size estimates obtained from magnetic measurements. The exception is catalyst γ-Fe_2O_3/Q-30, because the particle size exceeded single-domain range and could not be determined using the magnetic method.

Table 2. Iron oxide particle sizes found from Scherrer reflex width analysis.

Particle Size, nm			Catalysts
γ-Fe_2O_3	Fe_3O_4	α-Fe_2O_3	
		22	α-Fe_2O_3/Q-30
		13	α-Fe_2O_3/Q-15
		5	α-Fe_2O_3/Q-10
	24		Fe_3O_4/Q-30
	14		Fe_3O_4/Q-15
	7		Fe_3O_4/Q-10
25			γ-Fe_2O_3/Q-30
14			γ-Fe_2O_3/Q-15
8			γ-Fe_2O_3/Q-10

Figure 6. Diffraction patterns of catalysts (**a**) α-Fe$_2$O$_3$/Q-30, (**b**) Fe$_3$O$_4$/Q-30, (**c**) γ-Fe$_2$O$_3$/Q-30.

The phase transformations of nanoparticles occurring at all the stages of synthesis were investigated in more detail using Mossbauer spectroscopy.

To estimate the sizes of the obtained nanoparticles, spectra were measured at room temperature. Mathematical analysis of Mossbauer spectra of the samples obtained at all stages of synthesis allowed us to give a qualitative picture of the phase transformations taking place, to estimate the sizes of the obtained nanoparticles of iron oxides and to determine their quantitative characteristics. Particle size distributions for all investigated samples were also obtained from the mathematical processing of experimental Mossbauer spectra.

All the calculated parameters of the Mossbauer spectra are given in Table 3.

The Mossbauer spectrum of the α-Fe$_2$O$_3$/Q10 sample that was obtained at room temperature was a broadened paramagnetic doublet, characteristic of superparamagnetic compounds (Figure 7a).

Mathematical decomposition of the spectrum in Figure 7a revealed that it consisted of two components: a doublet of superparamagnetic α-Fe$_2$O$_3$ with particle sizes smaller than 10 nm [28,29] and a doublet of superparamagnetic α-FeOOH with particle sizes smaller than 5 nm [29]. To more precisely define both compounds' particle sizes, we measured the α-Fe$_2$O$_3$/Q10 sample at 77.5 K. The α-FeOOH component of the spectrum was still a superparamagnetic doublet at this temperature, which indicates the very small sizes of its nanoparticles (2–3 nm). The α-Fe$_2$O$_3$ component showed hyperfine magnetic splitting, corresponding to nanoparticles of 5–6 nm.

Table 3. Mossbauer spectra parameters (T = 300 K).

S, %	H_{eff}, kOe	Γ_{exp}, mm/s	Δ, mm/s	δ, mm/s	Phase	№	Sample
48		0.45	0.65	0.35	α-Fe$_2$O$_3$ d~6 nm	1	α-Fe$_2$O$_3$/Q-10
52		0.65	0.94	0.33	α-FeOOH(Si) d~2 nm	2	
29	400	2	0	0.27	Fe$_3$O$_4$ d~9 nm	1	Fe$_3$O$_4$/Q-10
55		0.62	0.76	0.35	Fe$_3$O$_4$ d~7 nm	2	
15		0.68	1.14	0.31	γ-Fe$_2$O$_3$ d~5 nm	3	
43	452	2	0	0.27	γ-Fe$_2$O$_3$ d~9 nm	1	γ-Fe$_2$O$_3$/Q-10
44		0.65	0.76	0.34	γ-Fe$_2$O$_3$ d~7 nm	2	
13		0.68	1.1	0.31	γ-Fe$_2$O$_3$ d~5 nm	3	
76		0.47	0.69	0.34	α-Fe$_2$O$_3$ d~11 nm	1	α-Fe$_2$O$_3$/Q-15
24		0.67	1.1	0.3	α-FeOOH(Si) d~2 nm	2	
33	440	1.2	0.5	0.35	Fe$_3$O$_4$ d~14 nm	1	Fe$_3$O$_4$/Q-15
51		0.76	0.92	0.37	Fe$_3$O$_4$ d~8 nm	2	
16		0.6	2.8	1.14	γ-Fe$_2$SiO$_4$ d~9 nm	3	
59	451	2	0	0.27	γ-Fe$_2$O$_3$ d~14 nm	1	γ-Fe$_2$O$_3$/Q-15
33		0.78	0.84	0.34	γ-Fe$_2$O$_3$ d~11 nm	2	
8		0.68	1.1	0.31	γ-Fe$_2$O$_3$ d~8 nm	3	
53	507	0.36	−0.22	0.37	α-Fe$_2$O$_3$ d~17 nm	1	α-Fe$_2$O$_3$/Q-30
29		0.45	0.66	0.34	α-Fe$_2$O$_3$ d~12 nm	2	
18		0.68	1.1	0.31	α-FeOOH(Si) d~2 nm	3	
49	452	0.6	0.02	0.64	Fe$_3$O$_4$ d~29 nm	1	Fe$_3$O$_4$/Q-30
	483	0.46	0	0.26	Fe$_3$O$_4$ d~29 nm		
13	420	1	−0.03	0.45	Fe$_3$O$_4$ d~15 nm	2	
17		0.91	1.06	0.36	Fe$_3$O$_4$ d~8 nm	3	
21	485	0.36	0	0.32	γ-Fe$_2$O$_3$ d~27 nm	4	
33	497	0.45	−0.02	0.34	γ-Fe$_2$O$_3$ d~29 nm	1	γ-Fe$_2$O$_3$/Q-30
21	478	0.45	0	0.3	γ-Fe$_2$O$_3$ d~20 nm	2	
36	439	1.5	0	0.46	γ-Fe$_2$O$_3$ d~15 nm	3	
10		0.6	0.85	0.36	γ-Fe$_2$O$_3$ d~9 nm	4	
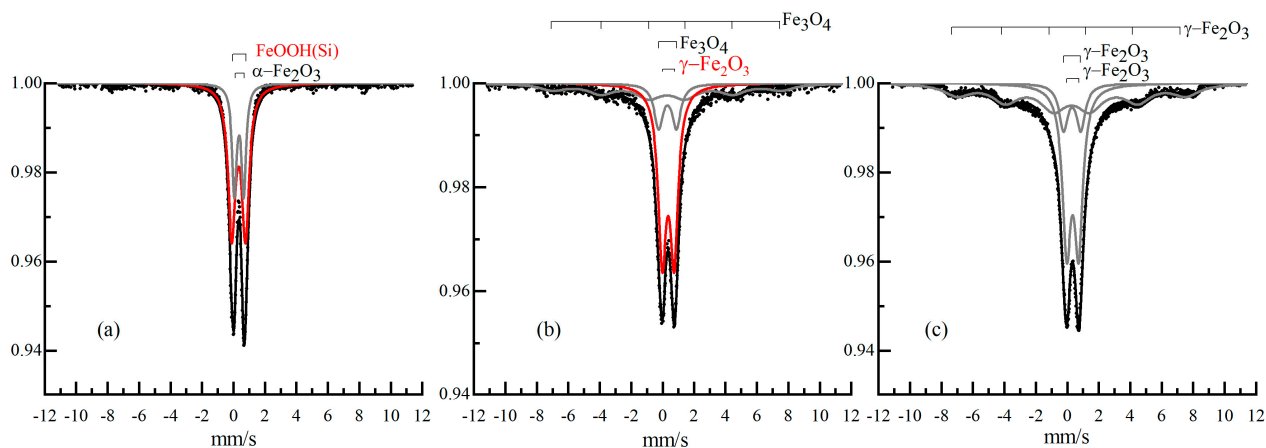
Figure 7. Mossbauer spectra of catalysts (**a**) α-Fe$_2$O$_3$/Q10, (**b**) Fe$_3$O$_4$/Q-10, (**c**) γ-Fe$_2$O$_3$/Q-10.

α-Fe$_2$O$_3$ nanoparticles of 5 nm and less in size have a number of atoms on the surface comparable to their number in volume. The reactivity of the surface atoms is thus so high that the atoms of the Fe-O chain at the particle surface interact with the OH-Si groups at the SiO$_2$-gel surface. As a result, nanolayers of goethite doped with silicon are formed on the surface of iron oxide nanoparticles, forming α-FeOOH(Si). The intensities of the α-FeOOH(Si) and α-Fe$_2$O$_3$ subspectra were 52 and 48%, respectively, which is consistent with the comparable number of atoms on the surface and in the volume of nanoparticles of ~5 nm and less.

At the second stage of the synthesis of Fe$_3$O$_4$/Q-10 nanosized particles, according to the X-ray data, the average particle size increased to 7 nm. In the Mossbauer spectrum in Figure 7b, this increase was manifested in the appearance of the Fe$_3$O$_4$ component with a hyperfine magnetic field of the relaxation type (H = 400 kOe). The superparamagnetic doublet of the Fe$_3$O$_4$ oxide formed the largest part of the spectrum (55%). In addition, the superparamagnetic component attributed to γ-Fe$_2$O$_3$ (15%) appeared. Apparently, it was due to the transformation of part of the α-FeOOH(Si) nanoparticles into γ-Fe$_2$O$_3$, which occurs during thermolysis of glucose at temperatures above 400 °C [30]. The peak on the thermomagnetic curve of the G/Fe$_2$O$_3$/Q-10 sample at 520 °C (Figure 1), as well as the Curie temperature shift beyond 600 °C, was due to this transformation. At the third stage of the synthesis of γ-Fe$_2$O$_3$/Q-10 nanoparticles, the average size of the formed γ-Fe$_2$O$_3$ nanosized particles further increased to 8 nm (Table 2). Analysis of the Mossbauer spectrum parameters showed that only γ-Fe$_2$O$_3$ nanoparticles with a narrow size distribution of 6–9 nm were formed in SiO$_2$/Q-10 pores (Figure 8c).
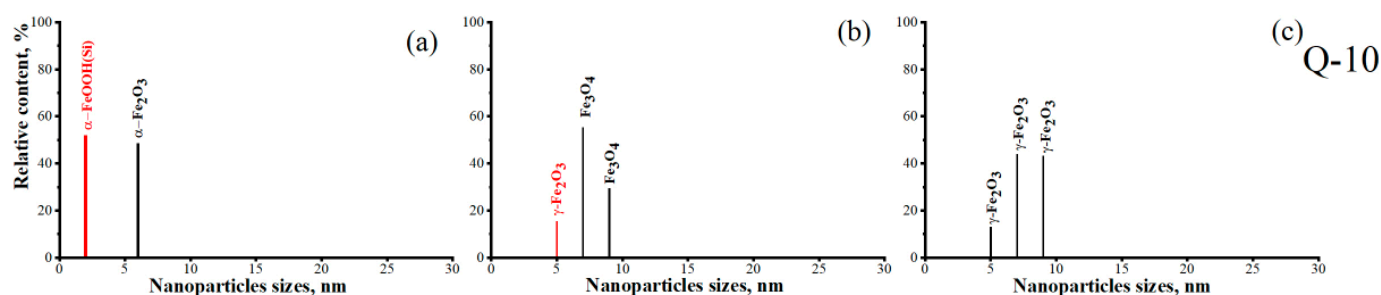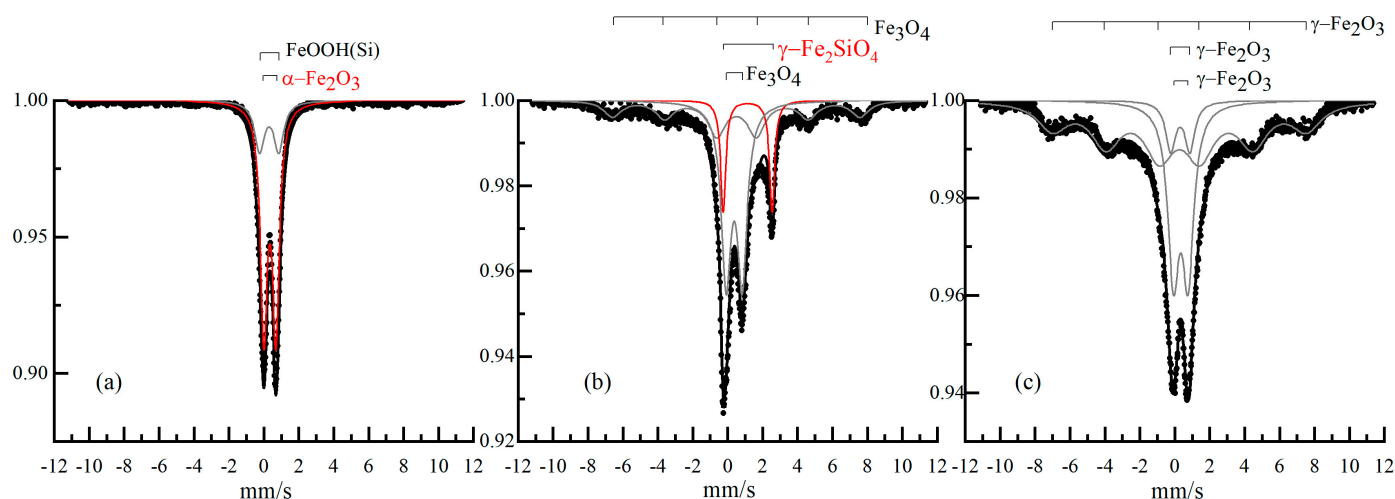

Figure 8. Size distribution diagrams for iron-containing components of catalysts (**a**) α-Fe$_2$O$_3$/Q-10, (**b**) Fe$_3$O$_4$/Q-10, (**c**) γ-Fe$_2$O$_3$/Q-10, where the intensities of the histograms correspond to the content of particles of a given size in the catalysts. The intermediate phases arising during the synthesis are marked in red.

In the SiO$_2$/Q-15 pores at all stages of γ-Fe$_2$O$_3$/Q15 synthesis, the nanoparticle sizes remained smaller than the pore size (Table 2). The sample formed at the first stage contained 76% α-Fe2O3 with particles of ~11 nm in size and 24% α-FeOOH(Si) with particles of ~2 nm in size. The Mossbauer spectra of catalysts α-Fe$_2$O$_3$/Q15 (a), Fe$_3$O$_4$/Q-15 (b) and γ-Fe$_2$O$_3$/Q-15 (c) are shown in Figure 9.

There were some features of phase transformations in the process of synthesis, however. The amount of α-FeOOH phase formed at the first stage of synthesis was two times less than in the case of α-Fe$_2$O$_3$/Q10 due to an increase in the average particle size to 7 nm and a reduction in the pore curvature. At the second stage, Fe$_3$O$_4$ particles were formed with most-probable sizes of around 8 and 14 nm. The contributions of these phases were 51 and 33%, respectively. Larger magnetite particles appeared in the spectrum as a relaxation-type component with a hyperfine magnetic field (H = 440 kOe). In addition, the second stage of Fe$_3$O$_4$/Q15 synthesis produced γ-Fe$_2$SiO$_4$ nanoparticles [31]. At the third stage of synthesis, only γ-Fe$_2$O$_3$ nanoparticles with a size distribution of 8–14 nm were formed in the Q-15 pores (Figure 10c). The main part was γ-Fe2O3 particles with a size of ~14 nm, and their share was 59%. The proportions of particles with sizes of ~11 nm and ~8 nm were 33 and 8%, respectively. We can see that for γ-Fe2O3/Q-15, the relative abundance of particles increased in direct proportion to their most probable size.

Figure 9. Mossbauer spectra of catalysts α-Fe$_2$O$_3$/Q15 (**a**), Fe$_3$O$_4$/Q-15 (**b**), γ-Fe$_2$O$_3$/Q-15 (**c**).
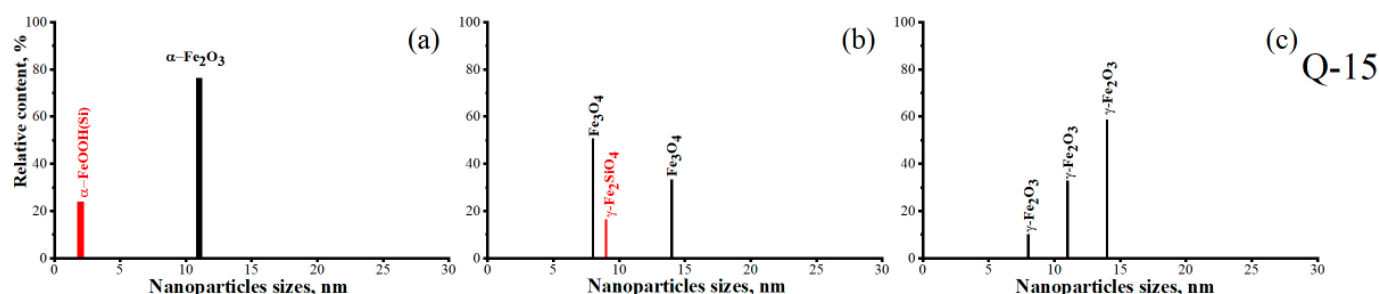
Figure 10. Size distribution diagrams for iron-containing components of catalysts (**a**) α-Fe$_2$O$_3$/Q-15, (**b**) Fe$_3$O$_4$/Q-15, (**c**) γ-Fe$_2$O$_3$/Q-15 obtained at the stages of synthesis of the γ-Fe$_2$O$_3$/Q-15 nanocatalyst.

A large number of antiferromagnetic α-Fe$_2$O$_3$ nanosized particles were initially formed in the SiO$_2$/Q-30 pores (Figure 11a), whose sizes approached the size of the single-domain state (the effective magnetic field parameter in the Mossbauer spectrum was 507 kOe). In addition, a number of smaller α-Fe$_2$O$_3$ nanoparticles were formed. About 20% of the spectrum was α-FeOOH(Si) phase, which was 2–3 nm in size. It should be noted that the Mossbauer parameters of the α–FeOOH(Si) phase formed at the first stage of synthesis were identical for all pore sizes. This is proof of the formation of an identical thin shell around the α-Fe$_2$O$_3$ particles in all the pores. It was this phase that was transformed into γ-Fe$_2$O$_3$ at the second stage of synthesis (Figures 11b and 12b). All α-Fe$_2$O$_3$ nanoparticles turned into Fe$_3$O$_4$. At the third stage of synthesis (Figure 11c), all the nanoparticles were transformed into γ-Fe$_2$O$_3$ with a broad nanoparticle size distribution of 9–29 nm (Figure 12c).

The average sizes of the nanoparticles of the obtained catalysts, estimated from the size distributions of the nanoparticles (Figure 12), were d = 7 nm for catalyst γ-Fe$_2$O$_3$/Q-10, d = 11 nm for γ-Fe$_2$O$_3$/Q-15, d = 25 nm for γ-Fe$_2$O$_3$/Q-30.

The dependences of magnetization on the magnetic field and pore sizes of catalysts γ-Fe$_2$O$_3$/Q-30, γ-Fe$_2$O$_3$/Q-15 and γ-Fe$_2$O$_3$/Q-10 were investigated by obtaining magnetization curves (Figure 13).

When a magnetic field is applied, particles with different relaxation times of magnetic moment (i.e., with different sizes) reach saturation magnetization at different values of the applied field, which leads to features in the γ-Fe$_2$O$_3$ magnetization curve.
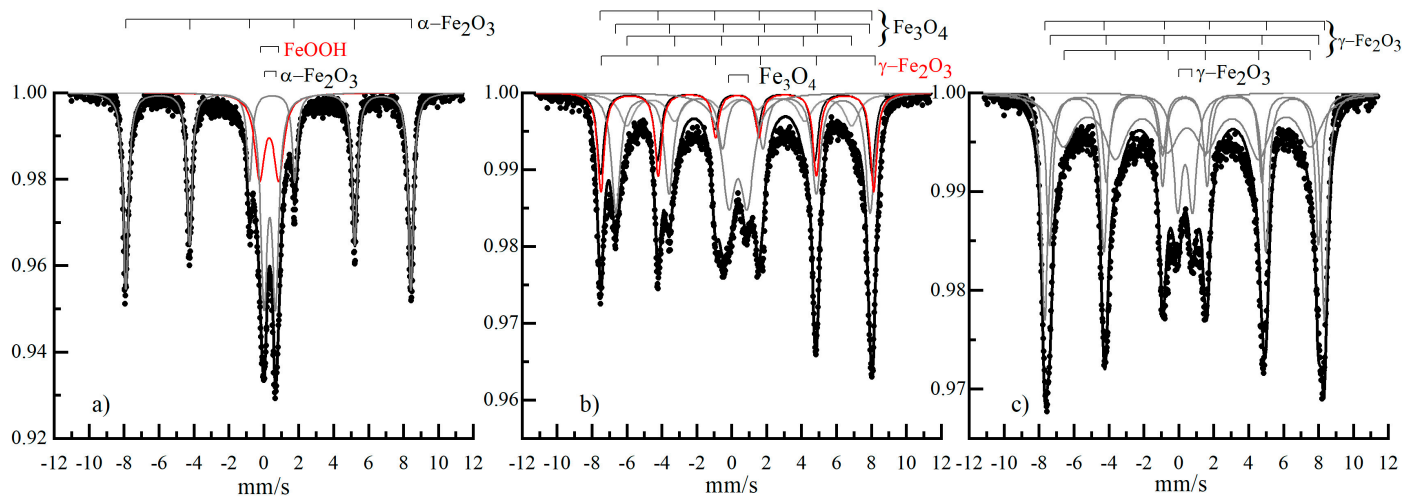
Figure 11. Mossbauer spectra of catalysts α-Fe$_2$O$_3$/Q30 (**a**), Fe$_3$O$_4$/Q-30 (**b**), γ-Fe$_2$O$_3$/Q-30 (**c**).
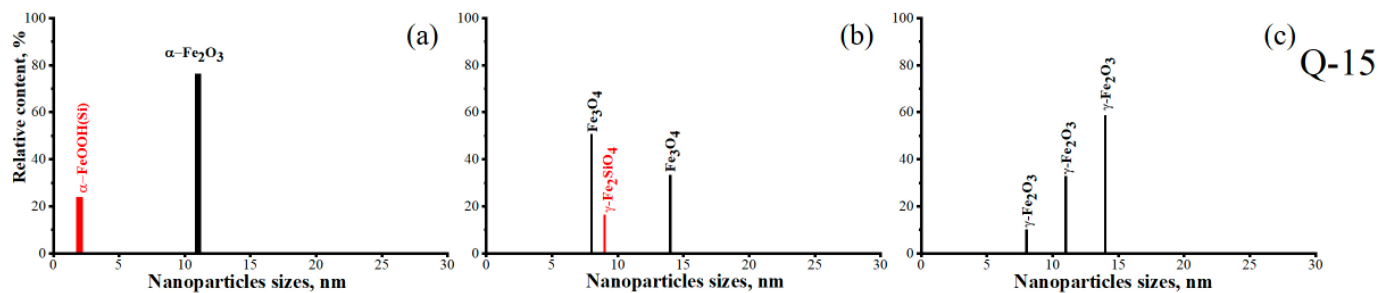
Figure 12. Size distribution diagrams for iron oxide nanoparticles obtained at the stages of synthesis of the γ-Fe$_2$O$_3$/Q-30 nanocatalyst: α-Fe$_2$O$_3$/Q-30 (**a**), Fe$_3$O$_4$/Q-30 (**b**), γ-Fe$_2$O$_3$/Q-30 (**c**).

Figure 13. The dependences of magnetization on the field and pore sizes of catalysts γ-Fe$_2$O$_3$/Q-30 (9–29 nm), γ-Fe$_2$O$_3$/Q-15 (8–14 nm) and γ-Fe$_2$O$_3$/Q-10 (6–9 nm).

The features of the curve are most clearly seen on the line related to γ-Fe$_2$O$_3$/Q-30, where the particle size distribution is the widest.

4. Conclusions
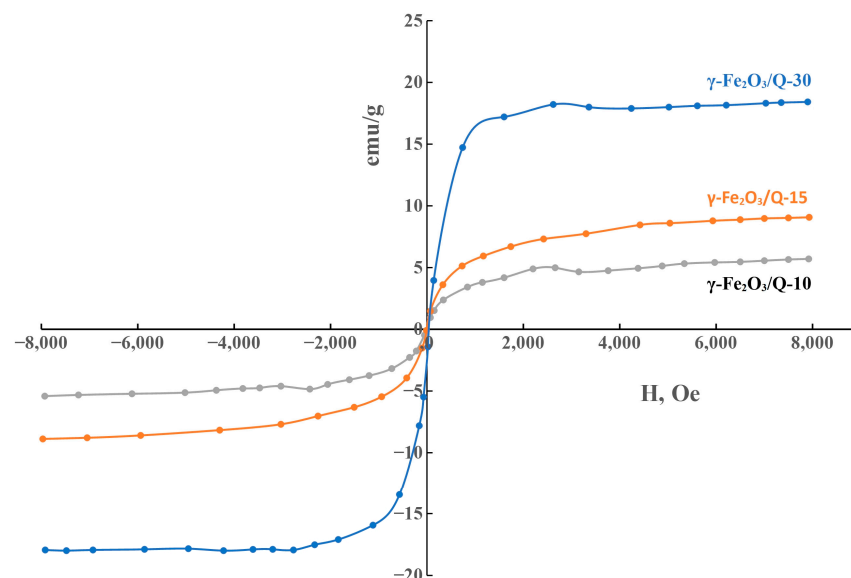
Based on the results of the present study, it can be concluded that the proposed chemical method for the synthesis of nanosized particles of iron oxides based on thermal reduction/oxidation in the presence of glucose is effective and promising for the synthesis of nanocatalysts with controlled particle sizes and their composition. Obviously, the carbon monoxide formed during glucose thermolysis contributes to the reduction of nanosized hematite particles on the surface of porous silica gel with the formation of nanosized magnetite particles. The subsequent oxidation of magnetite nanoparticles supported on silica gel for all catalysts leads to the formation of a single-phase system of nanosized maghemite particles. It has been shown that both the phase composition and particle size of iron oxides formed at all stages of catalyst synthesis depend on the pore sizes in the silica gel structure.

γ-Fe$_2$O$_3$/Q nanocatalysts were obtained in pores of all sizes, while the sizes of the resulting nanoparticles were limited by the pore size. As the pore size increased, the size distribution of the nanoparticles expanded, which corresponds to a wider range of relaxation times of the superparamagnetic nanosized particles' magnetic moments, which, in turn, affected the values of the magnetization of the obtained nanosized catalysts (Figure 13). We hope to more carefully study these magnetization curves after removing the temperature dependences of all the obtained nanocatalysts' Mossbauer spectra in the temperature range of 77.5–300 K. It will allow us to determine the relaxation times of magnetic moments for nanocatalyst particles of different sizes and the temperatures that block their magnetic state. The values of these parameters will make it possible to explain all the features of the magnetization curves.

References

1. Chourpa, I.; Douziech-Eyrolles, L.; Ngaboni-Okassa, L.; Fouquenet, J.-F.; Cohen-Jonathan, S.; Souce, M.; Marchais, H.; Dubois, P. Molecular composition of iron oxide nanoparticles, precursors for magnetic drug targeting, as characterized by confocal Raman microspectroscopy. *Analyst* **2005**, *130*, 1395. [CrossRef] [PubMed]
2. Jain, T.K.; Morales, M.A.; Sahoo, S.K.; Leslie-Pelecky, D.L.; Labhasetwar, V. Iron Oxide Nanoparticles for Sustained Delivery of Anticancer Agents. *Mol. Pharm.* **2005**, *2*, 194. [CrossRef] [PubMed]
3. Laurent, S.; Forge, D.; Port, M.; Roch, A.; Robic, C.; Vander Elst, L.; Muller, R.N. Magnetic Iron Oxide Nanoparticles: Synthesis, Stabilization, Vectorization, Physicochemical Characterizations, and Biological Applications. *Chem. Rev.* **2008**, *108*, 2064. [CrossRef]
4. Batlle, X.; Perez, N.; Guardia, P.; Iglesias, O.; Labarta, A.; Bartolome, F.; Garcia, L.M.; Bartolome, J.; Roca, A.G.; Morales, M.P.; et al. Magnetic nanoparticles with bulklike properties (invited). *J. Appl. Phys.* **2011**, *109*, 07B524. [CrossRef]
5. Yuen, S.; Chen, Y.; Kubsh, J.E.; Dumeslc, J.A. Metal Oxide-Support Interactions in Silica-Supported Iron Oxide Catalysts Probed by Nitric Oxide Adsorption. *J. Phys. Chem.* **1982**, *86*, 3022. [CrossRef]
6. Vikesland, P.J.; Heathcock, A.M.; Rebodos, R.L.; Makus, K.E. Particle Size and Aggregation Effects on Magnetite Reactivity toward Carbon Tetrachloride. *Environ. Sci. Technol.* **2007**, *41*, 5277. [CrossRef]
7. Yamaguchi, D.; Furukawa, K.; Takasuga, M.; Watanabe, K. A Magnetic Carbon Sorbent for Radioactive Material from the Fukushima Nuclear Accident. *Sci. Rep.* **2014**, *4*, 6053. [CrossRef]

8. Yavuz, C.T.; Mayo, J.T.; Yu, W.W.; Prakash, A.; Falkner, J.C.; Yean, S.; Cong, L.L.; Shipley, H.J.; Kan, A.; Tomson, M.; et al. Low-field magnetic separation of monodisperse Fe_3O_4 nanocrystals. *Science* **2006**, *314*, 964. [CrossRef]

9. Tong, S.; Zhu, H.; Bao, G. Magnetic iron oxide nanoparticles for disease detection and therapy. *Materialstoday.* **2019**, *31*, 86. [CrossRef]

10. Ang, B.C.; Yaacob, I.I. Preparation of Maghemite-Silica Nanocomposites Using Sol-Gel Technique. *Adv. Mater. Res.* **2010**, *97–101*, 2140. [CrossRef]

11. Heng, Z.; Schenk, J.; Spreitzer, D.; Wolfinger, T.; Daghagheleh, O. Review on the Oxidation Behaviors and Kinetics of Magnetite in Particle Scale. *Steel Res. Int.* **2021**, *92*, 2000687. [CrossRef]

12. Dragomir, B.B.; Lang, X.; Mukesh, D.; Zimmerman, W.H.; Rosynek, M.P.; Li, C. Binder/support effects on the activity and selectivity of iron catalysts in the Fischer-Tropsch synthesis. *Ind. Eng. Chem. Res.* **1990**, *29*, 1588. [CrossRef]

13. Shesterkina, A.A.; Shuvalova, E.V.; Redina, E.A.; Kirichenko, O.A.; Tkachenko, O.P.; Mishin, I.V.; Kustov, L.M. Silica-supported iron oxide nanoparticles: Unexpected catalytic activity in hydrogenation of phenylacetylene. *Mendeleev Commun.* **2017**, *27*, 512. [CrossRef]

14. Martínez, F.; Calleja, G.; Melero, J.A.; Molina, R. Iron species incorporated over different silica supports for the heterogeneous photo-Fenton oxidation of phenol. *Appl. Catal. B Environ.* **2007**, *70*, 452. [CrossRef]

15. Chernavskii, P.A.; Kazak, O.; Pankina, G.V.; Ordomsky, V.V.; Khodakov, A.Y. Mechanistic Aspects of the Activation of Silica-Supported Iron Catalysts for Fischer–Tropsch Synthesis in Carbon Monoxide and Syngas. *ChemCatChem* **2016**, *8*, 390. [CrossRef]

16. de Smit, E.; Weckhuysen, B.M. The renaissance of iron-based Fischer–Tropsch synthesis: On the multifaceted catalyst deactivation behavior. *Chem. Soc. Rev.* **2008**, *37*, 2758. [CrossRef]

17. Chen, L.; Costa, E.; Kileti, P.; Tannenbaum, R.; Lindberg, J.; Devinder, M. Sonochemical Synthesis of Silica-Supported Iron Oxide Nanostructures and Their Application as Catalysts in Fischer–Tropsch. *Synthesis. Micro* **2022**, *2*, 632. [CrossRef]

18. Ponomar, V.P.; Dudchenko, N.O.; Brik, A.B. Reduction roasting of hematite to magnetite using carbohydrates. *Int. J. Miner. Process.* **2017**, *164*, 21. [CrossRef]

19. Zhou, Y.; Yin, G.; Zeng, X.; Zhao, J.; Yao, G. Potential application of carbohydrate biomass in hydrometallurgy: One-pot reduction of metal oxides/salts under mild hydrothermal conditions. *RSC Adv.* **2022**, *12*, 20747. [CrossRef]

20. Ikoma, S.; Ohki, K.; Yokoi, H. Preparation and Characterization of Silica-Supported Maghemite. *J. Ceram. Soc. Jpn.* **1992**, *100*, 864. [CrossRef]

21. Paul, K.G.; Frigo, T.B.; Groman, J.Y.; Groman, E.V. Synthesis of Ultrasmall Superparamagnetic Iron Oxides Using Reduced Polysaccharides. *Bioconjugate Chem.* **2004**, *15*, 394. [CrossRef]

22. Chernavskii, P.A.; Lunin, B.S.; Zakharyan, R.A.; Pankina, G.V.; Perov, N.S. Experimental setup for investigating topochemical transformations of ferromagnetic nanoparticles. *Instr. Exp. Tech.* **2014**, *57*, 78. [CrossRef]

23. Barbier, A.; Hanif, A.; Dalmon, J.-A.; Martin, G.A. Preparation and characterization of well-dispersed and stable Co/SiO_2 catalysts using the ammonia method. *Appl. Catal. A Gen.* **1998**, *168*, 333. [CrossRef]

24. Kemp, S.J.; Ferguson, R.M.; Khandhar, A.P.; Krishnan, K.M. Monodisperse magnetite nanoparticles with nearly ideal saturation magnetization. *RSC Adv.* **2016**, *6*, 77452. [CrossRef]

25. Reichel, V.; Kovács, A.; Kumari, M.; Bereczk-Tompa, É.; Schneck, E.; Diehle, P.; Pósfai, M.; Hirt, A.M.; Duchamp, M.; Dunin-Borkowski, R.E.; et al. Single crystalline superstructured stable single domain magnetite nanoparticles. *Sci. Rep.* **2017**, *7*, 45484. [CrossRef] [PubMed]

26. Hadadian, Y.; Masoomi, H.; Dinari, A.; Ryu, C.; Hwang, S.; Kim, S.; Cho, B.; Lee, J.Y.; Yoon, J. From Low to High Saturation Magnetization in Magnetite Nanoparticles: The Crucial Role of the Molar Ratios between the Chemicals. *ACS Omega* **2022**, *7*, 15996. [CrossRef] [PubMed]

27. Cao, D.; Li, H.; Pan, L.; Li, J.; Wang, X.; Jing, P.; Cheng, X.; Wang, W.; Wang, J.; Liu, Q. High saturation magnetization of γ-Fe_2O_3 nano-particles by a facile one-step synthesis approach. *Sci. Rep.* **2016**, *6*, 32360. [CrossRef] [PubMed]

28. Bocquet, S.; Pollard, R.J.; Cashion, J.D. Dynamic magnetic phenomena in fine-particle goethite. *Phys. Rev.* **1992**, *B46*, 11657. [CrossRef]

29. Vandenberghe, R.E.; Barrero, C.A.; da Costa, G.M.; Van San, E.; De Grave, E. Mössbauer characterization of iron oxides and (oxy)hydroxides: The present state of the art. *Hyperfine Interact.* **2000**, *126*, 247. [CrossRef]

30. Hanesch, M.; Stanjek, H.; Petersen, N. Thermomagnetic measurements of soil iron minerals: The role of organic carbon. *Geophys. J. Int.* **2006**, *165*, 53. [CrossRef]

31. O'Neill, H.S.C.; McCammon, C.A.; Canil, D.; Rubie, D.C.; Ross, C.R., II; Seifert, F. Mössbauer spectroscopy of mantle transition zone phases and determination of minimum Fe^{3+} content. *Am. Miner.* **1993**, *78*, 456.